



**HAL**  
open science

## Mathematical Modeling of Energy-Dense NMC Electrodes: I. Determination of Input Parameters

Tuan Tu Nguyen, Bruno Delobel, Maxime Berthe, Benoît Fleutot, Arnaud Demortière, Charles Delacourt

► **To cite this version:**

Tuan Tu Nguyen, Bruno Delobel, Maxime Berthe, Benoît Fleutot, Arnaud Demortière, et al.. Mathematical Modeling of Energy-Dense NMC Electrodes: I. Determination of Input Parameters. *Journal of The Electrochemical Society*, 2022, 169 (4), pp.040546. 10.1149/1945-7111/ac653a . hal-03638931

**HAL Id: hal-03638931**

**<https://hal.science/hal-03638931>**

Submitted on 29 Apr 2022

**HAL** is a multi-disciplinary open access archive for the deposit and dissemination of scientific research documents, whether they are published or not. The documents may come from teaching and research institutions in France or abroad, or from public or private research centers.

L'archive ouverte pluridisciplinaire **HAL**, est destinée au dépôt et à la diffusion de documents scientifiques de niveau recherche, publiés ou non, émanant des établissements d'enseignement et de recherche français ou étrangers, des laboratoires publics ou privés.



Distributed under a Creative Commons Attribution 4.0 International License



# Mathematical Modeling of Energy-Dense NMC Electrodes: I. Determination of Input Parameters

Tuan-Tu Nguyen,<sup>1,2</sup> Bruno Delobel,<sup>2</sup> Maxime Berthe,<sup>5</sup> Benoît Fleutot,<sup>1,3</sup>  
Arnaud Demortière,<sup>1,3,4</sup> and Charles Delacourt<sup>1,3,z</sup> 

<sup>1</sup>Laboratoire de Réactivité et Chimie des Solides (LRCS), CNRS UMR 7314, Université de Picardie Jules Verne, Hub de l'Énergie, Rue Baudelocque, 80039 Amiens Cedex, France

<sup>2</sup>Renault Technocentre, 78084 Guyancourt, France

<sup>3</sup>Réseau sur le Stockage Electrochimique de l'Énergie (RS2E), CNRS FR 3459, Hub de l'Énergie, Rue Baudelocque, 80039 Amiens Cedex, France

<sup>4</sup>ALISTORE-European Research Institute, CNRS FR 3104, Hub de l'Énergie, Rue Baudelocque, 80039 Amiens Cedex, France

<sup>5</sup>Univ. Lille, CNRS, Centrale Lille, Univ. Polytechnique Hauts-de-France, JUNIA-ISEN, UMR 8520 - IEMN, F-59000 Lille, France

Physics-based models of the Li-ion battery are promising to decipher and quantify the electrode limitations, thereby providing valuable insights for choosing the optimal electrode design for a specific application. However, to obtain relevant results from the models, a reliable set of input parameters is required. This work presents a combined experimental/modeling approach relying on the Newman pseudo-2D model for a complete characterization of a set of  $\text{LiNi}_{0.5}\text{Mn}_{0.3}\text{Co}_{0.2}\text{O}_2$  electrodes. Intrinsic properties of the active materials are determined and validated using low-loading electrodes having negligible porous-electrode limitations. Then, high-energy-density electrode properties are characterized using appropriate experimental methods, which are widely reported in the literature. In the second part of this series of papers, parameters obtained from this part serve as input parameters in the Newman pseudo-2D model as well as in its extension in order to simulate the rate capability during discharge of the aforementioned set of high-energy-density electrodes.

© 2022 The Author(s). Published on behalf of The Electrochemical Society by IOP Publishing Limited. This is an open access article distributed under the terms of the Creative Commons Attribution 4.0 License (CC BY, <http://creativecommons.org/licenses/by/4.0/>), which permits unrestricted reuse of the work in any medium, provided the original work is properly cited. [DOI: 10.1149/1945-7111/ac653a]



Manuscript submitted January 24, 2022; revised manuscript received March 22, 2022. Published April 25, 2022.

Supplementary material for this article is available [online](#)

## List of symbols

$a_i$	$\text{m}^2/\text{m}_{\text{PE}}^3$	interfacial surface area of phase $i$
$c_{\text{s, surf}}$	$\text{mol m}^{-3}$	concentration at the surface of the AM particle
$c_{\text{s, max}}$	$\text{mol m}^{-3}$	maximum concentration of intercalated Li in AM particle
$c_{\text{s}}$	$\text{mol m}^{-3}$	solid-phase Li concentration within the AM particle
$\bar{c}_{\text{s}}$	$\text{mol m}^{-3}$	local volume-averaged solid Li concentration of AM phase within the PA
$c$	$\text{mol m}^{-3}$	salt concentration in a binary electrolyte
$d_{50}$	$\mu\text{m}$	median diameter of AM particles
$D$	$\text{m}^2 \text{s}^{-1}$	bulk diffusion coefficient of the liquid phase
$D_{\text{s}}$	$\text{m}^2 \text{s}^{-1}$	diffusion coefficient of Li in the AM particles
$F$	$\text{C mol}^{-1}$	Faraday's constant
$i$		coexisting phase presented in the PE
$i_{\text{n}}^0$	$\text{A m}^{-2}$	exchange current density
$i_{\text{Li}}^0$	$\text{A m}^{-2}$	exchange current density at the Li foil
$I_{\text{app}}$	$\text{A}/\text{m}_{\text{CC}}^2$	discharge current density
$j_{\text{n}}$	$\text{mol}/(\text{m}_{\text{AM}}^2 \cdot \text{s})$	pore-wall flux across the sandwich
$k_0$	$\text{mol} [\text{m}^2 \cdot \text{s} \cdot (\text{mol m}^{-3})^{1.5}]^{-1}$	reaction rate constant of the AM
$k_{0, \text{Li}}$	$\text{mol} [\text{m}^2 \cdot \text{s} \cdot (\text{mol m}^{-3})^{0.5}]^{-1}$	reaction rate constant of Li foil
$L_{\text{el}}$	$\mu\text{m}$	PE thickness
$L_{\text{sep}}$	$\mu\text{m}$	separator thickness
$Q_{\text{th}}$	$\text{Ah kg}^{-1}$	electrode theoretical capacity
$R$	$\text{J} (\text{mol} \cdot \text{K})^{-1}$	ideal gas constant
$r$	$\mu\text{m}$	radial dimension along the AM particle
$T$	$\text{K}$	absolute temperature
$t$	$\text{s}$	time
$t_{+}^0$		transference number of $\text{Li}^{+}$ in the electrolyte with respect to the solvent velocity
$U$	$\text{V}$	equilibrium potential of the AM

(Continued).

$\Delta V$	V	voltage drop between the two inner contacts in the $\mu 4$ -probe experiment
$x$	$\mu\text{m}$	dimension across the sandwich
$x_0$		initial stoichiometry
<b>Greek Symbols</b>		
$\alpha$		thermodynamic factor
$\beta$		charge transfer coefficient
$\varepsilon$	$\text{m}_{\text{elyte}}^3/\text{m}_{\text{PE}}^3$	PE porosity
$\varepsilon_{\text{sep}}$	$\text{m}_{\text{elyte}}^3/\text{m}_{\text{sep}}^3$	separator porosity
$\kappa_{\text{eff}}$	$\text{S m}^{-1}$	effective ionic conductivity of the liquid phase
$\rho_{\text{el}}$	$\text{g cm}^{-3}$	electrode density
$\sigma_{\text{eff}}$	$\text{S m}^{-1}$	effective electronic conductivity of the solid phase of the electrode
$\tau_{\text{Br}}$		tortuosity factor by Bruggeman
$\tau_{\text{e}}$		electrode tortuosity factor
$\tau_{\text{sep}}$		tortuosity factor of the separator
$\Phi_{\text{Li, Li}}$	V	electric potential at Li foil
$\Phi_i$	V	electric potential of phase $i$

The  $\text{LiNi}_x\text{Mn}_y\text{Co}_{(1-x-y)}\text{O}_2$  (NMC) electrode features high theoretical capacity, high energy density, structural stability, and high intrinsic rate capability that offer many potential advantages over existing active materials (AM). While progress has been continuously achieved to get even better AMs,<sup>1–5</sup> industry engineers and academic researchers keep working on making improvements at the electrode scale. This can be done through the electrode microstructure design, which has a substantial role in achieving high-performance Li-ion battery (LiB) electrodes. In general, the interplay between electrode microstructure and its performance is investigated through electrochemical measurements along with physics-based model analyses.<sup>6–9</sup> Recently, many works have also relied on tomography techniques to get additional insights directly from the 3D electrode microstructure.<sup>10–17</sup>

Obviously, densification of the electrode and/or increase in coating thickness significantly improve its volumetric energy density. In addition, the overall AM amount increases with coating thickness as the electrolyte, separator and current collector content decrease relatively, which can be a benefit for gravimetric energy density at the cell level up to the pack level. However, the search for optimal design is not straightforward because of the complex interplay between the microstructure and the different processes occurring during battery operation that affect the electrode performance. Understanding this interplay, therefore, is key for the optimization process of the electrode design.

For this purpose, the common approach currently relies on a trials-errors process using experimental testing. The drawback is that it generates little knowledge and understanding of what really happens in a device or during a process. It also requires a considerable amount of measurements with different configurations to be carried out so as to obtain reliable data for investigation. Instead, numerical modeling is promising and potentially a more time-efficient alternative to provide valuable insights for electrode design optimization. Among the different approaches to building a numerical model, physics-based models are based on the use of mathematical equations that represent the underlying physics. Providing the input parameters can be accurately determined, battery physics-based models enable predicting what is happening inside a cell in terms of, e.g., local state-of-charge and temperature, electric potentials of the solid and liquid phase, electronic and ionic current densities, and solid/liquid lithium concentration gradients. Moreover, rate-limiting factors can also be quantified through model analysis.

Among LiB continuum models, the so-called Newman pseudo-2D (P2D) model<sup>18–20</sup> offers the best compromise between computation speed and physical significance. It relies on porous electrode theory and concentrated solution theory.<sup>21</sup> However, such a detailed model requires a number of input parameters, describing each

component's morphology, kinetics, transport and thermodynamics, which are not straightforward to determine. Therefore, one crucial part of physics-based models is parameterization. Without an exact knowledge of the individual material parameters, statements about internal states are only possible to a minimal extent.

Some works have made great efforts to tackle this issue and shed light on the parameterization methodology.<sup>9,22–27</sup> In Refs. 24, 25 and 27, the parameterization was done on electrodes from commercial cells. Although microstructural properties such as the tortuosity factor and the electronic conductivity can be directly quantified from these electrodes, given their moderate-to-high loading, porous electrode limitations can affect the determination of active-material properties. Instead, for active-material characterization, electrochemical techniques (e.g. PITT, GITT) on low-loading electrodes with negligible porous-electrodes effects were demonstrated to be appropriate.<sup>22,23,26</sup>

Overall, reliable input parameters from literature are still limited. Consequently, in most works dealing with physics-based models, some key parameters are fitted or even assumed in order to match the experimental results. For instance, Colclasure et al.<sup>28</sup> investigated the limitations of extreme fast charging for NMC/Graphite cells with high loading electrodes using Newman P2D model with adjusted solid-diffusion coefficients for both active materials.

Furthermore, results from the parametrization process are still of interest to the modeling community, which relies on physics-based models to get valuable insights from the performance of porous electrodes (PE).<sup>9,24,25,28–32</sup> For instance, Usseglio-Viretta et al.<sup>33</sup> proposed a relationship between porosity and tortuosity factor for NMC electrodes, whereas Malifarge et al.<sup>9</sup> proposed the same for Graphite electrodes. Other works with similar materials and/or electrode designs can use one of those relationships to calculate tortuosity-factor values.

With this in mind, in this first part of this series of papers, we aim to tackle the parametrization process with a set of carefully designed experiments carried out on a set of NMC electrodes including industry-grade and lab-made low loading electrodes. The validation for active-material properties is performed on lab-made electrodes. In the second part, the Newman P2D model along with its extension that accounts for particle agglomerates are investigated for the validation of the discharge rate capabilities of four different industry-grade electrodes.

## Model Theory

In this work, since lithium metal is used in place of a porous negative electrode, a half-cell is modeled. The model consists of one NMC electrode and one separator domains, whereas only the outer surface of the Li foil and the current collector of the NMC electrode

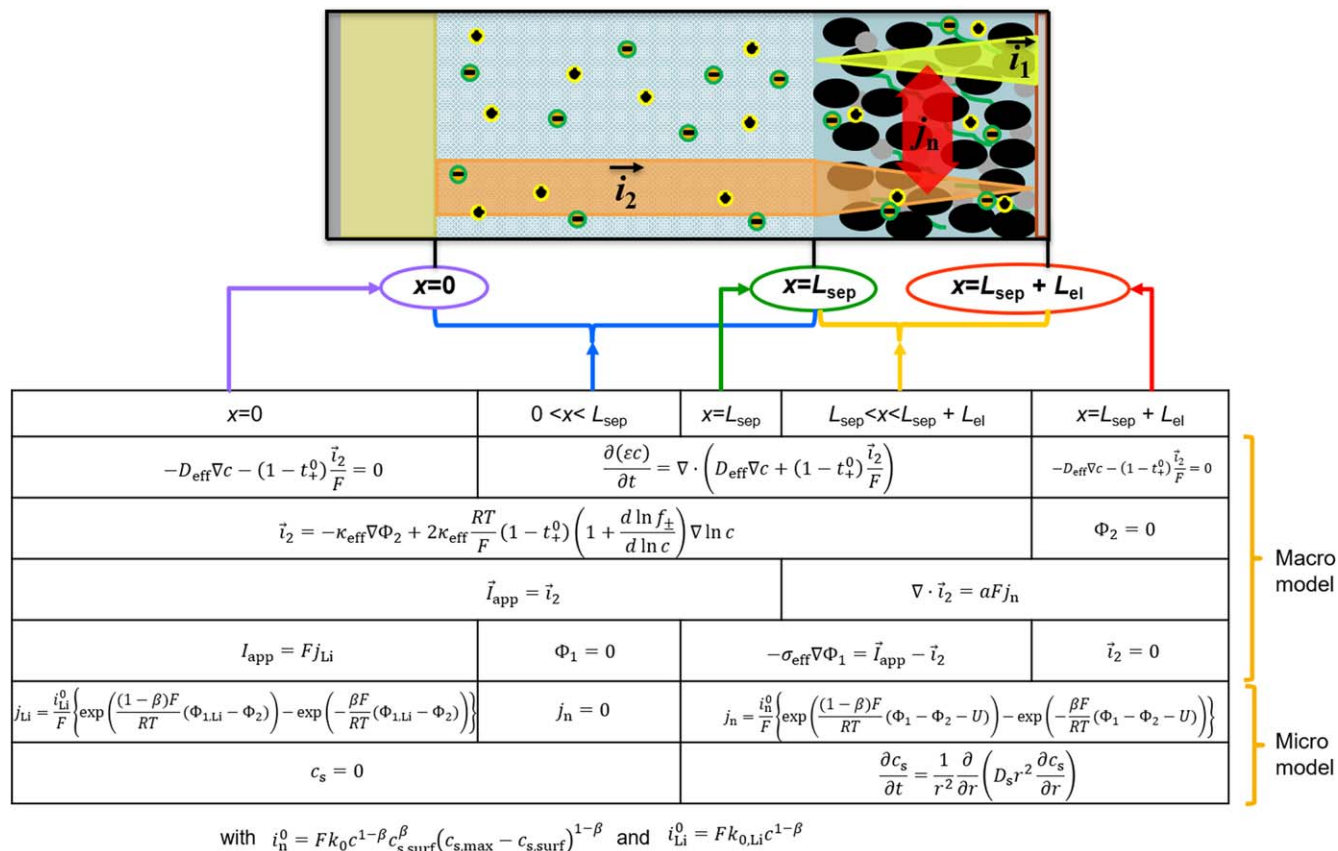


**Figure 1.** Half-cell model (Li foil/PE) derived from the Dualfoil model, which was developed by Newman’s research group in the 1990’s. Model equations and boundary conditions are provided in the table. Note that boundary conditions for the bottom equation (spherical diffusion in the active particles) are not indicated, for conciseness.

are represented through their boundary with the separator and the electrode, respectively, for the sake of simplicity.

**Newman P2D model.**—Newman P2D model is a physics-based model of the anode/separator/cathode elementary sandwich (Dualfoil). The model equations and various model features are described in detail.<sup>17</sup> The model is based on the porous electrode theory. That is, the PE is treated as a superposition of two continua that are considered to coexist at every point within the electrode. There is one continuum representing the solid mixture including AM, conductive carbon, and polymeric binder, and another one representing the liquid phase (electrolyte). Moreover, the exact geometry details of all the particles and pores in the electrode are disregarded, as they are considered as small enough compared to the volume element dimensions. Instead, each coexisting phase  $i$  is ascribed macro-homogenous parameters such as its volume fraction  $\varepsilon_i$ ; its interfacial surface area,  $a_i$ ; and an electrode tortuosity factor,  $\tau_e$ .

The model is 1D + 1D (or P2D), i.e., there is a dimension  $x$  across the sandwich (“macro” model), and a radial dimension  $r$  along the AM particles that are assumed spherical and isotropic (“micro” model).

Figure 1 illustrates different domains represented by the Newman P2D model adapted for the half-cell (Li foil/PE) along with the set of equations. Each equation is represented within the domain where it is applied to. Boundary conditions are also shown, except for the boundary conditions for solid diffusion in the active particles.

In the “macro” model, an electronic current density flowing across the PE thickness in the solid phase is represented by Ohm’s law, while an ionic current density flows similarly in the liquid phase and is expressed according to a Mac-Innes equation, that considers both ohmic and concentration overpotentials. The mass balance is

applied to the anion (e.g.,  $\text{PF}_6^-$ ), which has an identical concentration as the cation by virtue of electroneutrality. The anion flux density is treated with concentrated solution theory. The ionic and electronic current densities are linked through the so-called pore-wall flux of Li, representing the rates of the electrochemical reactions at solid/liquid interface, expressed with Butler-Volmer kinetics.

In the “micro” model, the Li concentration distribution within the AM particles is obtained by solving for a mass balance on “neutral” Li, i.e. the bipolar  $\langle \text{Li}^+, e^- \rangle$  pairs. When the thermodynamic factor is taken as unity as a first approximation, the material balance simplifies to Fick’s second law.

The “macro” model connects with the “micro” model through the pore-wall flux of  $\text{Li}^+$ . While the “micro” model relates to the active-material intrinsic properties, the “macro” model rather reflects the microstructural properties of the electrode. Thus, if the “micro” model can accurately represent the particle behavior, one may want to study the “macro” model to optimize the electrode design.

In the Newman P2D model, a total of *ca.* 20 parameters is required to compute the simulations. Overall, there are six independent variables, namely the salt concentration in the electrolyte (assumed binary),  $c$ ; the solid-phase Li concentration within the AM particle,  $c_s$ ; the pore-wall flux,  $j_n$ ; the ionic current density in the liquid phase,  $i_2$ ; the electric potential of the solid phase,  $\Phi_1$ ; the electric potential of the liquid phase,  $\Phi_2$ ; which are defined at each node along the elementary sandwich (and at each node across the particles for  $c_s$ ) at each time. A control volume formulation is used to solve for the set of differential and algebraic equations across the sandwich. More details on the solution procedure may be found in Refs. 17, 18.

The Newman P2D model is simulated with DUMBAT,<sup>34</sup> a physics-based modeling software for Li-ion cell simulations. Later in the second part of this series of papers, we develop a new model that uses the polynomial approximation<sup>35</sup> as an approximate solution

**Table I. Theoretical composition, porosity, thickness (without Al current collector), AM loading and density of NMC electrodes used in this work.**

Sample	Content	Porosity ( $\epsilon$ )	Thickness	AM loading	Density
	%w NMC/CB/Binder	$\text{m}^3/\text{m}_{\text{PE}}^3$	$\mu\text{m}$	$\text{mg cm}^{-2}$	$\text{g cm}^{-3}$
	%v NMC/CB/Binder				
MX-01	96.0/2.2/1.8 90.0/5.0/5.0	0.212	74.4	25	3.5
MX-02	96.0/2.2/1.8 90.0/5.0/5.0	0.280	48.8	15	3.2
MX-01b	94.2/3.2/2.6 86.0/7.0/7.0	0.191	74.4	25	3.5
MX-02b	94.2/3.2/2.6 86.0/7.0/7.0	0.191	44.6	15	3.5

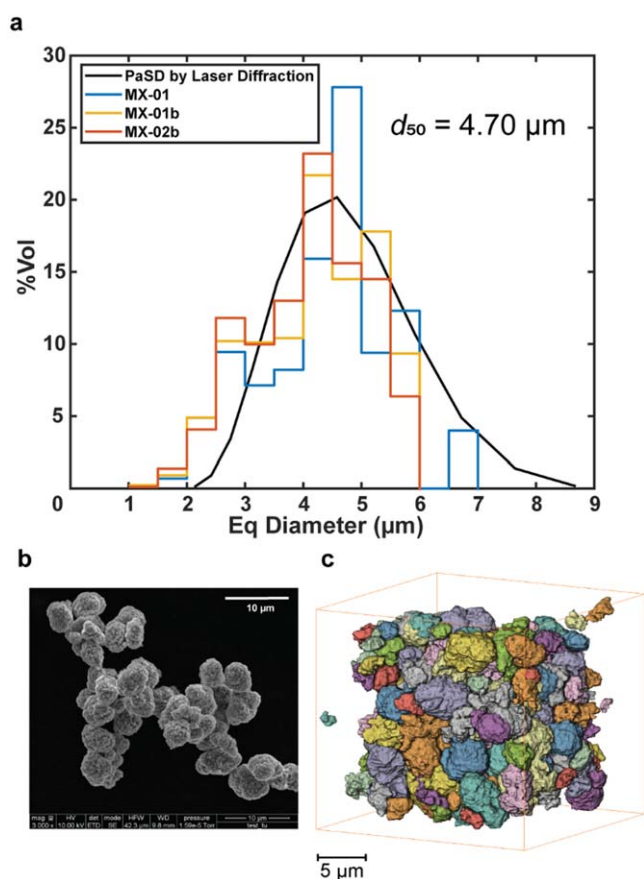


**Figure 2.** Morphology of the AM phase. (a). PaSD of the NMC used as AM characterized by Laser diffraction on raw powder and X-ray Holotomography on electrodes. (b). SEM photo of NMC powder. (c). The NMC in an electrode captured by X-ray Holotomography is separated into individual particles that allow the statistical analysis of the microstructural properties by particles.

to solve the solid diffusion in AM particles. Compared with the regular Newman P2D model, this approximation allows removing the additional dimension across the particle radius. Therefore, for the sake of comparison between the two models, we also introduce the Newman model using polynomial approximation hereafter. For ease of understanding, it is referred to as the Newman-pa model, whereas the regular Newman P2D model is denoted as the Newman P2D model here below.

### Experimental

**NMC electrode preparation.**—Four different industry-grade positive electrodes are investigated in this work and labelled as

MX-01, MX-02, MX-01b, and MX-02b. Each electrode is a mixture of  $\text{LiNi}_{0.5}\text{Mn}_{0.3}\text{Co}_{0.2}\text{O}_2$  (NMC532) as AM, conductive carbon black (CB) and a mixture of polyvinylidene fluoride (PVdF) with a co-binder as additives with various compositions and loadings. They are all calendered to reach the targeted high-density values. Their specifications from supplier's datasheet are shown in Table I.

**Particle size distribution.**—The particle size distribution (PaSD) of the raw NMC532 particles is determined with the laser diffraction method using the Mastersizer 3000 particle size analyzer and its state-of-art dry dispersion system. The PaSD is obtained from the angular variation in the intensity of light scattered as a laser beam passes through a dispersed particulate sample. Large particles scatter light at small angles relative to the laser beam and small particles scatter light at large angles. The angular scattering intensity data is then analyzed to calculate the size of the particles responsible for creating the scattering pattern, using the Mie theory of light scattering. As for output, laser diffraction will give a volume-weighted distribution of particle diameter, which is calculated with the volume-equivalent sphere diameter.

**Lab-made thin electrode fabrication.**—The mixture of AM and carbon black is first pre-mixed for 12 h before adding binder dispersed in NMP using a Polytron PT10–35 homogenizer. Two different formulations are used with different compositions: 94/3.2/2.8 and 96/2/2 corresponding to %wt AM/CB/PVdF respectively. The slurry is cast on an 18  $\mu\text{m}$  thick battery-grade aluminum (Al) foil. After being dried overnight in the dry room at room temperature, only uniform regions of the electrode are calendered using a rolling mill and their thickness is measured to an accuracy of 1  $\mu\text{m}$  with a digital Palmer. The measured thicknesses are ca. 7 to 12  $\mu\text{m}$ , ranging from two to four layers of NMC particles on the current collector.

**Coin cell fabrication.**—The electrodes are punched from the laminates to 1.3 cm diameter disks. The weight and thickness are measured for each electrode, so that electrode porosity and specific capacity are calculated for each coin cell. The electrodes are dried completely under vacuum at 120 °C for 8–10 h before coin-cell assembling. The coin cells are assembled inside an argon-filled glove box in standard 2032 coin-cell hardware. A lithium metal disk of 200  $\mu\text{m}$  thickness and of 1.4 cm diameter is used as the counter electrode without any surface treatment. The counter electrode is pressed on a 0.5 mm stainless steel spacer. A Celgard 2500 separator of 1.65 cm is placed on top of the Li foil. 100  $\mu\text{l}$  of different electrolytes are then added to soak the separators. Three electrolytes are used in this work to unveil different limitation sources, as discussed later in the text. The LP30 1 M refers to the 1 mol  $\text{l}^{-1}$  solution of lithium hexafluorophosphate ( $\text{LiPF}_6$ ) in ethylene carbonate (EC)/dimethyl carbonate (DMC) (1:1 w). The LP40 1 M refers to the 1 mol  $\text{l}^{-1}$  solution of lithium hexafluorophosphate ( $\text{LiPF}_6$ ) in EC/diethyl carbonate (DEC) (1:1 w). Finally, the same mixture is used but with a lower concentration (0.5 M), hereafter referred to as

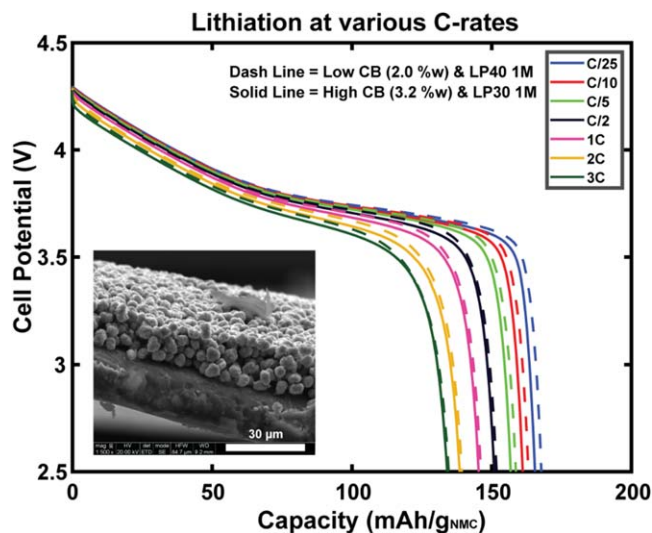


**Figure 3.** Rate capabilities of two thin electrodes. Both are made with different compositions (%w AM/CB/PVdF: 96/2/2 vs 94/3.2/2.8) and filled with different electrolytes (LP40 1 M vs LP30), respectively.

“LP40” 0.5 M. Lastly, the cathode is placed on top of the separator. The cell is then crimped closed with a hydraulic crimping machine.

**Electrochemical measurements.**—All measurements are carried out in a controlled temperature chamber at 25 °C. It is worth mentioning that isothermal condition is applied throughout the discharge rate capability tests, as one focuses on the effects of the electrode microstructure on its power performance. However, temperature dependency of the system can be explored in the future using the model, which is of interest to industry-oriented applications. The cycling tests are performed with a multipotentiostat (Bio-logic, France). The potential window for the NMC materials in this work is between 2.5 and 4.3 V vs Li/Li<sup>+</sup>. All the electrochemical results were performed using the thin electrode having low carbon black (2.0%wt) unless specifically described. For this electrode, 1 C current corresponds to a current density of 4.52 A m<sup>-2</sup>.

All coin cells first undergo a formation process in which they are cycled five times with constant-current (CC) discharge/charge cycles at C/10 to form a stable passive layer at the particle surface as well as for Li foil to further cycle on already cycled Li. A constant voltage (CV) is held at the end of the discharge of the fifth cycle until the current gets down to C/50. This extra step before further charging is to ensure that the electrode discharge is complete (close to pristine state). Finally, a CCCV charge followed by a CC discharge is carried out, both at C/25, for capacity determination. The available capacity is determined at the end of the CC discharge.

The rate-capability experiments are conducted on two separate coin cells using the same electrode to ensure repeatable results. Upon both charge and discharge, a CCCV protocol is used, where the cells are cycled with different currents (C/25, C/10, C/5, C/2, 1 C, 2 C, and 3 C). During the CV steps, the cell potential is held constant at both cut-off voltages until the current gets down to C/50. Between each change of current, the cell is idled for 1 h to allow for some relaxation.

For the potentiostatic intermittent titration technique (PITT), the cell potential is stepped by 10 mV increments from 2.5 and 4.3 V and vice-versa. Each individual titration (at a potential step) is held until the current decreases to C/200 (in magnitude).

For the tortuosity factor determination of the pore space, the symmetric cell method is used, which is reported by Landesfeind et al.<sup>36</sup> and Malifarge et al.<sup>37</sup> The coin cells are assembled with identical cathodes at both sides of a separator, filled with a blocking electrolyte (10 mM of TBAClO<sub>4</sub> in EC:DMC (1:1 w) solvent). Two stainless-steel spacers of 1 mm instead of 0.5 mm are used to

compensate for the lower thickness of the cathode compared to a Li foil, so that an appropriate pressure inside the cell is ensured. The Electrochemical Impedance Spectroscopy (EIS) of the cells is measured using MTZ frequency analyzer from Bio-logic. The measurements are carried out at two different temperatures (25 °C and 10 °C). The change in temperature changes the ratio between the effective ionic and electronic conductivity of the liquid and solid phase respectively as the ionic conductivity is more temperature-dependent than the electronic conductivity. It is a simple way to assess whether the electronic conductivity can be safely ignored for the correct determination of the electrode tortuosity factor. If the electrode tortuosity factor value is consistent at both temperatures, no electronic conductivity measurement is needed to analyze data from the symmetric cell. In addition, the experiments are conducted on two separate coin cells using the same electrode to ensure that the results are reproducible.

For electronic conductivity determination, EIS is performed using a 4-line configuration. This configuration ensures that measured conductivities are independent of the contact resistances between the probes and the sample, which are known to vary depending on the applied pressure of the probes onto the sample. The temperature is set to vary within a range [−20 °C, 60 °C], allowing for the extraction of activation energy for the electronic conductivity. The measurements are carried out using an ITS system and a MTZ (Bio-logic, France).

Besides, to assess the local electronic conductivity, a direct current measurement is performed using the  $\mu$ 4-probe method.<sup>38–40</sup> When the 4 probes are aligned, the voltage drop  $\Delta V$  between the two inner contacts is measured, while a current  $I$  is injected through the two outer contacts, so that the ratio  $\frac{\Delta V}{I}$  is a measure of the sample resistance  $R$ . The 4 probes are part of a multiple-probe Scanning Tunneling Microscope, with SEM monitoring, allowing independent movement of each probe with nanometer precision. As a result, the distance between probes can be varied, then the measured scale also changes. Depending on the probing distance, the effective resistivity of the PE can be determined through equations in Table I in Ref. 35.

## Results & Discussion

**Parametrization results.**—Electrolyte properties as a function of Li concentration are reported by Lundgren et al.<sup>41</sup> and Landesfeind et al.<sup>42</sup> It is worth mentioning that in order to improve model prediction capability, we have extrapolated the LP40 properties from [0.5–1.5] mol l<sup>-1</sup> to [0–3] mol l<sup>-1</sup>, just like it was done by Malifarge et al.<sup>9</sup> Although one must be extremely cautious when extrapolating the electrolyte properties, the authors had no other choice but to use extrapolated data, given the missing solid measured data for LP40 electrolyte in the 0–0.5 and 1.5–3 M ranges. For the LP30, the experimental data was already reported over the range [0–3] mol l<sup>-1</sup>. Both electrolyte properties are presented in Fig. S1 (available online at [stacks.iop.org/JES/169/040546/mmedia](https://stacks.iop.org/JES/169/040546/mmedia)).

Values for the separator thickness and porosity are taken from the Celgard datasheet. Its tortuosity factor is determined by measuring the effective electrolyte conductivity by EIS (more details in Fig. S2).

The reaction-rate constant at the lithium foil was measured by Mastali et al.<sup>43</sup> It is determined from data analysis of a lithium symmetric cell cycled at various current densities. Similar experiments carried out in house yielded a similar value at 25 °C (not shown here).

Regarding the PE, a multi-modal approach combined with model analysis is required for complete characterization: transport properties (electronic/ionic conductivity), AM intrinsic properties (solid diffusion coefficient, reaction-rate constant). For AM, the variation of the solid diffusion coefficient with Li concentration is significant, especially as to the material gets close to a full lithiation state.<sup>23,26</sup> Thus, a variable diffusion coefficient is considered in this work for higher simulation accuracy. This is also applied to the reaction-rate constant.<sup>44</sup>

**Table II. Common parameters for the models used in this work (a: assumed, m: measured, \*: calculated).**

Parameters	Values
<b>LiNi<sub>0.5</sub>Mn<sub>0.3</sub>Co<sub>0.2</sub>O<sub>2</sub></b>	
Theoretical Capacity, $Q_{th}$	277 Ah kg <sup>-1</sup> *
Density, $\rho_{el}$	4740 kg m <sup>-3</sup> *
Initial stoichiometry, $x_0$	0.38 <sup>m</sup>
Particle diameter, $d_{50}$	4.7 $\mu\text{m}$ <sup>m</sup>
Charge transfer coefficient, $\beta$	0.5 <sup>a</sup>
<b>Li foil</b>	
Li metal reaction rate, $k_{Li}^0$	6.64 10 <sup>-6</sup> mol/[m <sup>2</sup> ·s·(mol m <sup>-3</sup> ) <sup>0.5</sup> ] <sup>43</sup>
<b>Separator</b>	
Porosity, $\epsilon_{sep}$	0.55 <sup>45</sup>
Tortuosity factor, $\tau_{sep}$	6.8 <sup>m</sup>
Thickness, $L_{sep}$	25 $\mu\text{m}$ <sup>45</sup>
<b>Electrolyte</b>	
LiPF <sub>6</sub> in EC:DEC (1:1 w)	Lundgren (2014) <sup>41</sup>
LiPF <sub>6</sub> in EC:DMC (1:1 w)	Landesfeind (2019) <sup>42</sup>

Despite the authors' effort to build the model from the root, solid diffusion coefficient still needs to be adjusted from the work of Wu et al.<sup>26</sup> through the validation of the rate capability of the lab-made thin electrode. This will be discussed later in the paper. The common parameters for the models in this work are summarized in Table II.

**Particle size distribution.**—PaSD of AM measured by laser diffraction is presented as black line in Fig. 2, which possess a  $d_{50}$  of 4.7  $\mu\text{m}$ . The PaSD is divided into multiple intervals or bins (in this case, 12). The full PaSD (12 bins), as well as a binned PaSD (reduced to 5 bins) are used for simulations, and both show no substantial differences from simulation with one-particle size using the  $d_{50}$  value (Fig. S3). As a result, for simulation convenience (duration and convergence), one-particle size instead of multiple particle sizes is used for simulations.

Besides, the PaSD using tomographic data of MX-01, MX-01b and MX-02b from our previous work<sup>11</sup> are also presented in Fig. 2a, showing a good agreement with the laser diffraction experiment. The largest population of particles from three tomographic data correspond to the  $d_{50}$  from measurement, despite a slightly larger population of particles having a diameter of less than 3  $\mu\text{m}$ . Here, this can be due to the calendaring process, which is known to cause fractures of AM particles under high mechanical pressure resulting in smaller particles. The cracked AM particles can be clearly observed from the tomographic data.<sup>11</sup>

It is worth noting that the particle size is calculated after separating the NMC continuum phase into individual particles by means of a separation algorithm based on the contrast between image pixels. Besides, this allows the quantification of interconnectivity between an individual AM particle and other phases, which will be used in the second part of this work in an extension of Newman model that accounts for the contact between AM/AM.

**Porous effects on low loading electrodes.**—As mentioned above, low loading electrodes are made in our laboratory using the same AM powder as that in the industry-grade electrodes under investigation. Thin electrodes are well-suited to the determination of intrinsic properties of AM, because the porous-electrode effects are alleviated, thereby increasing the sensitivity to solid diffusion and charge transfer.

Regarding the thin electrode characterization, its effective electronic conductivity cannot be measured properly with the 4-line method just like for higher-loading electrodes, since the aluminum foil cannot be removed without breaking the electrode due to its low loading. Also, the symmetric cell method is conducted first, to determine the electrode tortuosity factor. However, the EIS response does not agree well with theoretical expectations; a large semi-circle appears in the intermediate frequency range instead of a straight line with slope of *ca.* 45°. Consequently, the minor effects of porous-electrode limitations are experimentally assessed by comparing the rate capabilities of two thin electrodes with different compositions and porosity and that are filled with a different electrolyte (LP30 1 M or LP40 1 M). The geometric characteristics of the two electrodes are shown in Table III. Figure 3 shows a good agreement between the rate capabilities of the two electrodes, which confirms that porous-electrode effects are almost negligible. The thin electrodes are, therefore, appropriate for the determination of AM intrinsic properties, namely the reaction rate constant and the solid-diffusion coefficient.

**Solid diffusion coefficient & reaction rate constant.**—The NMC used in this work is intercalation compounds, the performance of which depends on the kinetics of charge transfer and the solid Li diffusion. These two processes are described in Newman-type models by two parameters, namely the reaction-rate constant  $k_0$  and the solid diffusion coefficient  $D_s$ . Numerous experimental methods were developed to determine them, e.g., PITT,<sup>22,46–50</sup> galvanostatic intermittent titration technique (GITT),<sup>23,26,51,52</sup> cyclic voltammetry (CV),<sup>53</sup> and electrochemical impedance spectroscopy (EIS).<sup>54,55</sup>

Here, the PITT is employed because it is well suited for fine screening of composition ranges in which the AM experiences a steep change in equilibrium potential with composition. For NMC, it is the region close to the full lithiation state that is known to experience the largest variation of the diffusivity.

In Fig. 4, the two parameters are determined from the PITT experiment on thin electrodes by combining it with Newman P2D model analysis, as used in many works.<sup>22,26,56</sup> They are estimated by matching the simulated and experimental current response during potential steps at different lithiation states using a least-square regression method.

Nonetheless, as discussed later, the solid-diffusion coefficient determined in this work does not provide a good agreement between the simulated and experimental rate capability of the thin electrode, despite decent fits of the current response during potential steps in PITT (see Fig. S4). Instead, we relied on the solid diffusion coefficient obtained from Fig. 6 in Ref. 26 with slight adjustments so as to better approach the experimental rate capability of the actual

**Table III. List of model parameters used for half-cell simulations at 25 °C of rate capability of the thin electrode. a: assumed value, m: measured value, \*: calculated from design.**

Parameters	Values	
Electrode	<b>3.2%w CB</b>	
Thickness, $L_{el}$	6.44 $\mu\text{m}$ <sup>m</sup>	7.57 $\mu\text{m}$ <sup>m</sup>
Porosity, $\epsilon$	0.41*	0.19*
Tortuosity factor of the liquid phase (Bruggeman), $\tau_{Br}$	0.41 <sup>-0.5</sup> a	0.19 <sup>-0.5</sup> a
Electronic conductivity, $\sigma_{eff}$	1000 S m <sup>a</sup>	1000 S m <sup>a</sup>
%v AM, $\Psi_{AM}$	0.51*	0.73*

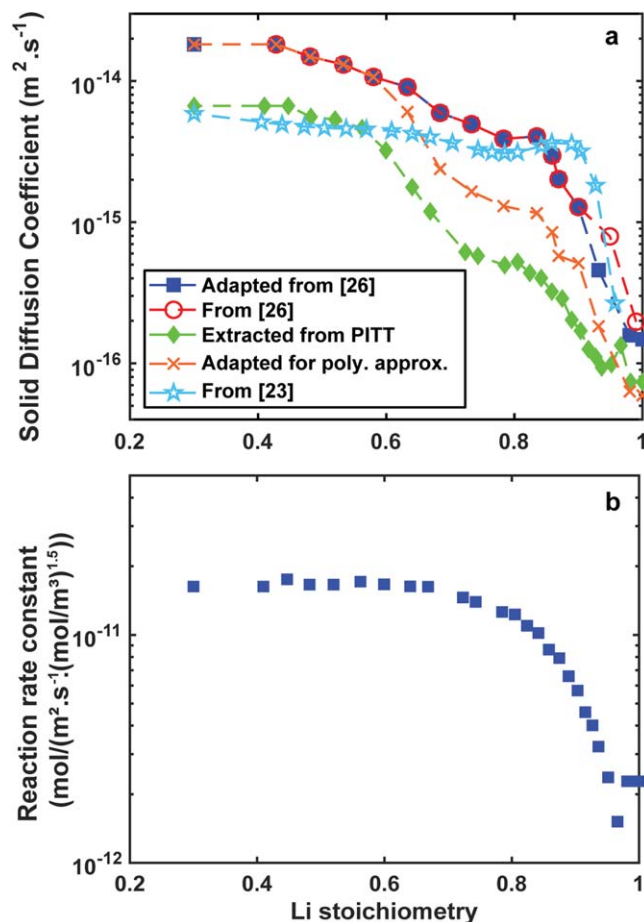


**Figure 4.** Intrinsic properties of the NMC used in this work. (a). The solid-diffusion coefficient extracted from PITT experiment along with four others: the original values from Wu et al.<sup>26</sup> and Verma et al.,<sup>23</sup> two sets of adjusted values to fit the rate capability of thin electrode from this work using either the Newman P2D model or the Newman-pa model. (b). The reaction rate constant extracted from PITT measurement.

thin electrode studied herein. For comparison,  $D_s$  reported by Wu et al.<sup>26</sup> for NMC111, and by Verma et al.<sup>23</sup> for NMC532, along with the  $D_s$  extracted from PITT in this work and the “adjusted”  $D_s$  used for the Newman P2D and the Newman-pa models, respectively, are all represented in Fig. 4a.

**Equilibrium potential.**—At the end of each potential step during the PITT experiments, the lithiation state within the NMC particles reaches quasi-equilibrium, as the current is lower than  $C/200$ . At that time, the cell potential is considered at equilibrium. Upon charge and discharge, two different equilibrium potential curves due to a residual hysteresis are obtained. Thus, the final equilibrium potential is taken as the average of the two curves.

On the other hand, we also consider a low-rate discharge ( $C/50$ ) to get the full lithiation state started from the initial stoichiometry  $x_0 = 0.38$  (i.e.,  $Li_{0.38}Ni_{0.5}Mn_{0.3}Co_{0.2}O_2$ ). This low-current potential profile, whenever used directly as input for the equilibrium potential, is more correctly labelled as a pseudo-equilibrium potential because the system is not at equilibrium.

Figure 5 compares the average equilibrium potential obtained from the PITT upon charge and discharge with the pseudo-equilibrium potential from the low-rate discharge at  $C/50$ . The discrepancy in terms of polarization between these two curves is minor. In other words, during a discharge at  $C/50$ , the system is very close to its thermodynamic stability. While the equilibrium potential averaged from PITT shows an abrupt drop toward the cut-off voltage

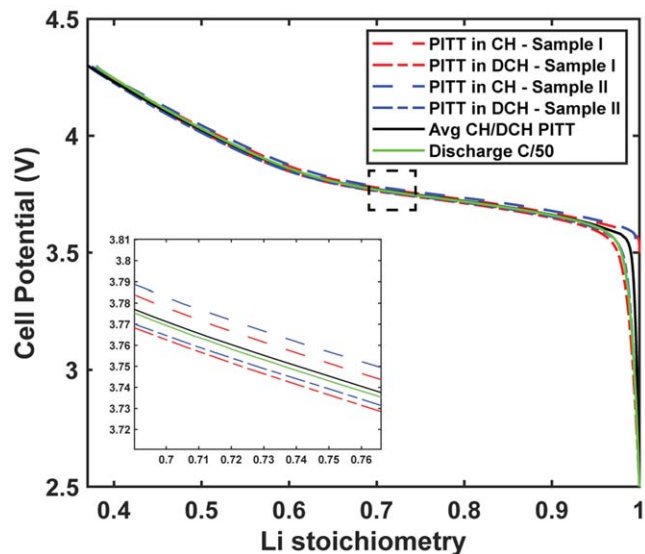


**Figure 5.** Equilibrium potential of the NMC used in this work. Different potential curves during the charge and discharge process extracted from PITT experiment along with the discharge curve at  $C/50$  are presented for comparison.

at the EoD, referred to as the “kink” region, both the PITT and the  $C/50$  in discharge represent a more gradual potential decline at the EoD. Therefore, as we focus on the discharge behavior of the electrodes, the discharge curve at  $C/50$  is rather considered hereafter as the pseudo-equilibrium potential to better capture this behavior.

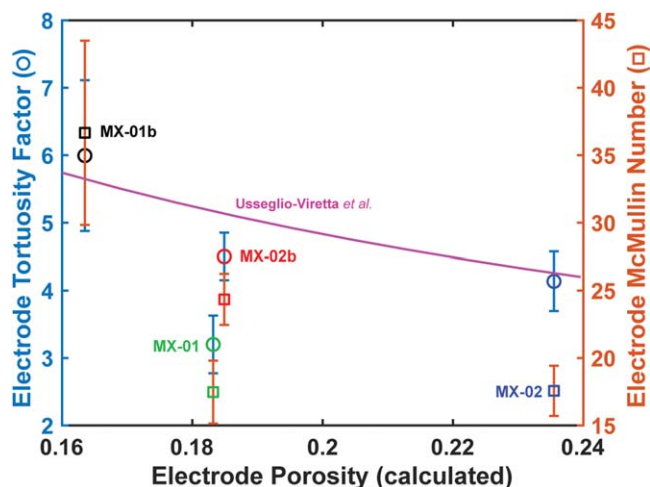
**Electrode tortuosity factor.**—The electrode tortuosity factors are measured with the symmetric cell method,<sup>36,37</sup> which has been demonstrated through experimental<sup>33,57</sup> as well as a numerical approaches<sup>58</sup> to be appropriate for the determination of tortuosity applied to porous electrodes.

Figure 6 shows the electrode tortuosity factor determined from the symmetric-cell method for the four industry-grade electrodes studied in this work. The results suggest negative effects of the carbon binder domain (CBD) on the electrode in terms of tortuosity, as MX-01b and MX-02b both yield higher electrode tortuosity factor values than MX-01, despite having similar porosities.

Notably, the results are in good agreement with the values calculated from the power-law reported by Usseglio-Viretta et al.<sup>33</sup> based on a fit of measured values using the same method for electrodes having similar NMC532 materials. Given that the porosity can slightly deviate ( $\pm 3\%$ ) from theoretical value due to a non-optimized manufacturing process, the McMullin number for each electrode is also represented in Fig. 6 (i.e., it corresponds to an electrode tortuosity factor “normalized” by its porosity).

Furthermore, Malifarge et al.<sup>37</sup> measured the electrode tortuosity factors of different graphite electrodes using a similar method (except for the use of a conventional LP40 electrolyte instead of a blocking salt) and found really good agreement between simulated and experimental rate capability of the electrodes by using measured tortuosities as model input. For graphite electrodes with similar porosity, they found that the electrode tortuosity factors range from 7 to 10. Since they studied graphite particles having a flake-like geometry, the electrodes are expected to be more tortuous than those with more spherical particles such as the NMC in this work. Therefore, the electrode tortuosity-factor values shown in Fig. 6 seem to be reasonable for industry-grade electrodes in this work.

Moreover, the simulations by *TauFactor*<sup>58,59</sup> using the tomographic data also give the values within the experimental ranges for MX-01b and MX-02, as shown in Fig. S5. The EIS responses of the four electrodes, along with the fit for tortuosity factor determination are shown in Fig. S6.



**Figure 6.** Electrode tortuosity factor and McMullin number. The average electrode tortuosity factors (o) of the 4 electrodes measured by the symmetric cell method are presented along with the average McMullin number calculated (□) for each electrode. The error bars represent the standard deviation of the parameters. For comparison, the value obtained by empirical power-law from Usseglio-Viretta et al.,<sup>33</sup> is also presented.

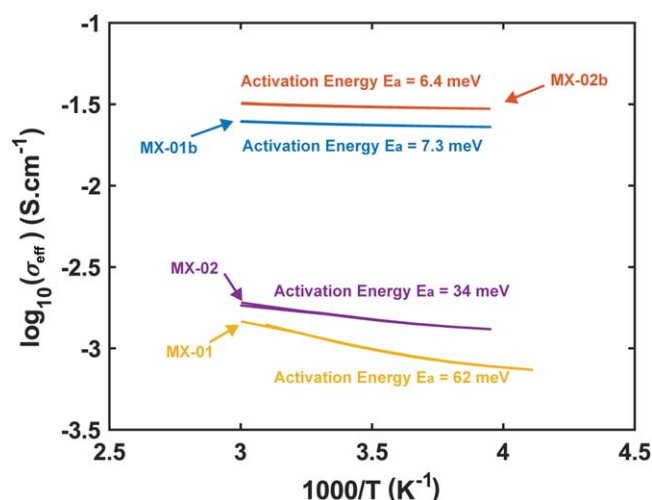


**Figure 7.** Electronic conductivities of the 4 industry-grade electrodes measured by the 4-line method as a function of the temperature.

**Electronic conductivity.**—For the electronic conductivity measurements, the 4-line method<sup>60</sup> is used instead of the 2-point method that highly depends on the compression pressure by the two sensing probes, which cannot be controlled with our equipment. The effective conductivity as a function of the temperature along with the activation energy for the four electrodes is shown in Fig. 7. The sensitivity of the conductivity measured by the 2-point method as a function of the compression pressure is shown in Fig. S7.

Besides, a  $\mu$ 4-probe method is also employed that allows for probing the electronic conductivity at various scales, as the probing distance can be adjusted using  $\mu$ -manipulators. Also, this study enables the mapping of the electronic conductivity at different locations throughout the electrode surface. A correlation between the local electronic conductivity and the electrode microstructure, measured at identical locations, is the scope of a future work. Several measurements were performed at different locations (without overlapping) to assess the microstructure heterogeneities, at each probing distance. The average/min/max  $\sigma_{\text{eff}}$  along with the 95% confidence intervals are presented in Fig. 8. As expected, a higher dispersion, i.e., larger error bar, of  $\sigma_{\text{eff}}$  is observed, as we go

to a lower scale, as it gets more sensitive to local microstructure. All values measured at the macro scale lie within the confidence intervals of the conductivity measured with the  $\mu$ -4-probe method at the lowest scale.

A higher amount of carbon additives (+1%wt.) shows a big improvement ( $\sim 10$ ) on the electronic conductivity of the electrode across multi-length scales. Also, the more carbon conductive in the sample, the higher the electronic conductivity and the lower the activation energy. The effective electronic conductivities of the porous electrodes lie between the bulk values of the carbon binder mixture ( $250\text{--}300\text{ S m}^{-1}$ )<sup>61</sup> and the NMC materials at a pristine state ( $0.00136\text{ S m}^{-1}$ ).<sup>62,63</sup> In a multi-phase porous structure, there likely is a mix of transport properties, so that the carbon additives and the NMC materials both contribute to the electronic transport throughout the electrodes. Given that the NMC electronic conductivity varies with the Li concentration, the electronic conductivity of the porous electrode may vary as a function of the SoC. Nevertheless, we notice here that the electronic conductivity is not a dominant limitation for these electrodes, since we will see in the second part of this work that the better electrochemical performances are generated by electrodes with lower electronic conductivities. Therefore, throughout our work, it is assumed that the electronic conductivities of the electrodes during operation can be represented by the values measured at a pristine state.

**Model validation against experimental results.**—In this section, the Newman P2D model is first used to validate the AM properties: reaction rate constant ( $k_0$ ) and solid diffusion coefficient ( $D_s$ ), in the framework of the thin electrodes.

Simulations for which local salt concentration reaches  $3\text{ mol l}^{-1}$  anywhere across the cell sandwich are interrupted. In this situation, simulated values of the cell overpotential may still serve for comparison with experiments, whereas values of the delivered capacity are irrelevant and discarded.

It is worth noting that the model may not describe properly the Li plating/stripping mechanism at the (assumed) flat Li foil. During operation, the Li foil/electrolyte interface might not be very flat due to moss and/or non-uniform distributed current density, which may lead to a lower-than-expected  $\text{Li}^+$  concentration in the vicinity of the foil. Consequently, at a high current density, the model can predict a higher  $\text{Li}^+$  concentration in the vicinity of the Li foil. Combined with the significant decrease of electrolyte properties at high concentration, the simulated discharge potential curve might show a fast drop and a much smaller EoD capacity than that observed in the experiments.

Fortunately, as demonstrated above, porous-electrode effects in the thin electrode are negligible. As a result, it is assumed that the thin electrode tortuosity factor follows Bruggeman's correlation, even though it is known to poorly predict the electrode tortuosity factor for the other electrodes studied here. Also, the effective electronic conductivity of the thin electrode is set to a high value, so that there is no ohmic drop across the electrode thickness. Table III shows the set of parameters used for the Newman P2D & Newman-pa models of the thin electrodes.

The parameters ( $D_s$ ,  $k_0$ ) and their dependency on solid Li concentration determined from PITT experiments on a thin electrode are taken into account in the Newman P2D model as a lookup table with linear interpolation, to simulate its rate capability for validation. Even though the current response during potential steps simulated by the Newman P2D model match well with the PITT experiment albeit perhaps close to full AM lithiation (see Fig. S4), Fig. 9a shows that the simulated rate capability does not match experimental data correctly. Despite the significant discrepancies in EoD capacity, the polarization of the electrode from simulations match well with the measurements (up to ca. 3 C in Fig. 9b). Therefore,  $k_0$  values from PITT are retained for the rest of the study. Conversely, the mismatch between simulated and experimental EoD capacity suggests values of  $D_s$  from PITT are not suitable for rate-capability simulations. Although the root cause of the discrepancy between simulation and

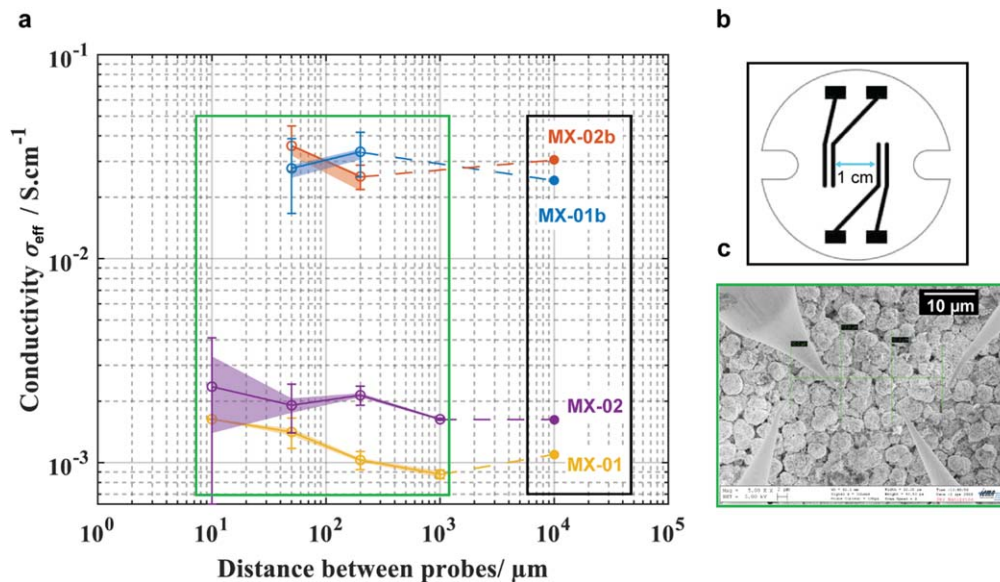


**Figure 8.** Multi-scale electronic conductivity. (a). The electronic conductivities of the 4 electrodes measured by two methods, 4-line (full circles in black box) and  $\mu$ 4-probe at different length scales (open circles in the green box), are presented. (b). Schematics of the electrode used in the 4-line method from Bio-logic, in which the 4 probes are made by gold deposit on a plastic substrate. c. SEM photo of the 4  $\mu$ -probes made by tungsten in the  $\mu$ 4-probe method.

experimental rate capability is not clarified, some hypotheses can be subject to further study in the future. In a 2-electrode system, there can be contributions from the Li foil to the current response in the PITT experiment in a more complicated way than the model accounts for. Also, the current range of PITT experiments is about  $\sim C/50$  (i.e.,  $0.09 \text{ A m}^{-2}$ ) in average, which may not be meaningful in order to fit C-rate as high as 20 C (i.e.,  $90.4 \text{ A m}^{-2}$ ) of the rate capability data. Complementary, GITT experiment on thin electrodes were also carried out. However, similar to the PITT experiment, despite the good quality of fitting the measured experimental data (voltage responses to current pulses), solid diffusion coefficient extracted from the GITT experiment could not validate the thin electrode discharge capability either.

The solid-diffusion coefficient,  $D_s$ , determined by Wu et al.<sup>26</sup> for NMC111 materials using GITT on a thin electrode combined with a model analysis, is used instead. To get a better match between simulations and experiments upon discharge rate capability,  $D_s$  is manually adjusted in the Li-rich composition range and turns out to decrease faster than that by Wu et al. for NMC111 as one approaches full lithiation.

Figure 10a shows a fair agreement between the simulated discharge curves and the experimental data, regarding both EoD capacity (Fig. 10b) and average polarization (Fig. 10c), over the entire range of discharge C-rates. Thus,  $D_s$  and  $k_0$  are then retained for modeling the industry-grade electrodes in the second part of this series of papers.

Nevertheless, the model cannot represent the gradual decline of cell potential toward the EoD, especially at high C-rates. Even with the use of the discharge curve at C/50 as an equilibrium potential rather than the averaging of PITT charge and discharge, the simulated potential drop near the EoD is much more sudden in the simulations than it is in the experimental data.

A possible reason for it is the distribution of the electronic resistance (e.g., electronic contact resistance between AM/CBD, electronic resistance across the AM) that would account for a distribution of the resistance for electron transport from the conductive electrode matrix all the way to the reaction sites.<sup>29</sup> Furthermore, the NMC conductivity is reported to decrease substantially once the materials get close to full lithiation state.<sup>64</sup> Consequently, considering a constant effective electronic conductivity during the entire operation might not be accurate enough to properly address the cell potential decline toward the EoD. Here, it is

decided not to focus on this minor discrepancy but electronic effects (distribution+stoichiometry dependence of AM conductivity) could be implemented in the mathematical model for a better model prediction capability in future work.

As seen in Figs. 11a–11c, the simulated liquid-phase concentration profile across the electrode thickness does not show any Li depletion issue.

In addition, Figs. 11b–11d show the volume-average Li utilization within the particles across the thickness of the electrodes, which is nearly uniform, even for C-rates as high as 10 C and 20 C. This justifies that the Li intercalation occurs uniformly across the electrode thickness, as expected if porous-electrode effects are negligible. Increasing the tortuosity factor at values well above that estimated from Bruggeman correlation also yields no effect on the particle utilization (not shown here).

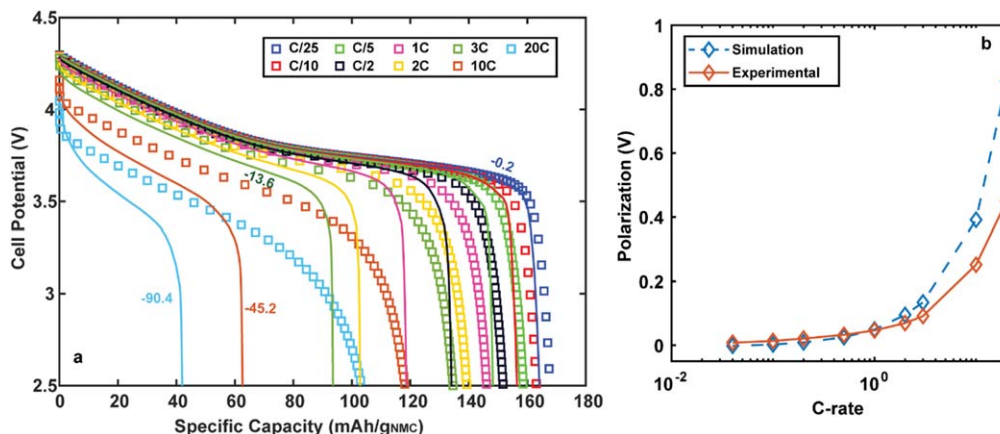
As mentioned above for the second part of this work, the polynomial approximation<sup>35</sup> is used as an approximate solution to solve the solid diffusion in AM particles for an extension of Newman model that accounts for particle agglomerates. As a result, the solid coefficient diffusion  $D_s$  is no longer taken as a function of  $c_s$ , but assumed to be a function of the volume-averaged concentration  $\bar{c}_s$  in the particles whenever the polynomial approximation is used. Thus,  $D_s$  must be re-adjusted to validate the rate capability on the thin electrode (orange curve in Fig. 4a), given the slight differences due to this different assumed concentration-dependence of  $D_s$  (Fig. S8).

Figure 12 represents the model/experiment comparison of the discharge rate capability of the thin electrode with the Newman-pa model using the new “fitted”  $D_s$ . On the other hand, the polarization from simulations shows good agreement to the experimental for the entire range of C-rates. Therefore,  $k_0$  is kept identical hereafter.

As a short conclusion, the validation step on the thin electrode without substantial porous-electrode effects, proves our set of parameter values is relevant for representing the AM intrinsic properties.

## Conclusions

In this work, an experimental/modeling approach relying on Newman P2D model is performed to characterize the porous NMC electrodes. It provides all parameters required for the parameterization of the physics-based macrohomogenous models that will be



**Figure 9.** Validation rate capability on low loading electrode. (a). The simulation of the rate capability of a thin electrode (solid lines) is compared with the experimental results (square markers). (b). Overpotential at  $\text{Li}_{0.77}\text{Ni}_{0.5}\text{Mn}_{0.3}\text{Co}_{0.2}\text{O}_2$  upon discharge from  $\text{Li}_{0.38}\text{Ni}_{0.5}\text{Mn}_{0.3}\text{Co}_{0.2}\text{O}_2$  in function of C-rates from experimental and simulation data. AM intrinsic properties ( $D_s$ ,  $k_0$ ) derived from the PITT measurement are used as model inputs. The current densities are in  $\text{A m}^{-2}$ . For the sake of clarity, we decided to not add all the current densities in the plot.

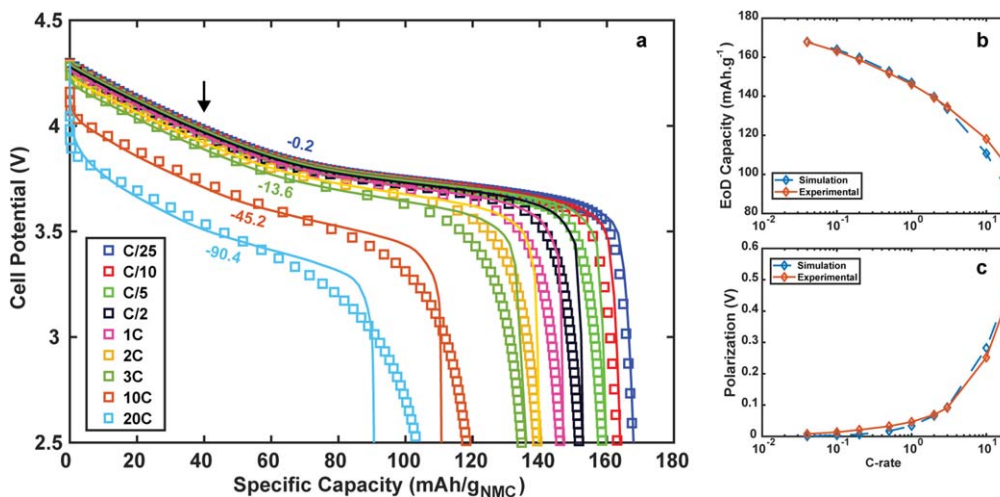


**Figure 10.** Validation rate capability on low loading electrode. (a). Discharge curves of a thin electrode at different current densities. (b). EoD capacity as a function of C-rate from experimental and simulation data. (c). Overpotential at  $\text{Li}_{0.77}\text{Ni}_{0.5}\text{Mn}_{0.3}\text{Co}_{0.2}\text{O}_2$  upon discharge from  $\text{Li}_{0.38}\text{Ni}_{0.5}\text{Mn}_{0.3}\text{Co}_{0.2}\text{O}_2$  (indicated by the black arrow) in function of C-rates from experimental and simulation data. The current densities are in  $\text{A m}^{-2}$ .

used in the second part for the validation of industry-grade electrodes.

Electrode properties such as the electrode tortuosity factor and the effective electronic conductivity are determined through appropriate experiments directly on industry-grade electrodes. The electrode tortuosity factor shows a good agreement when comparing to the values from the literature for similar electrodes using the same methods. The measured values of the effective electronic conductivity of the electrode materials show large dispersion when going down to the micro-scale, indicating local heterogeneities within the electrode microstructure. Overall, electrodes with 1%wt. of carbon additives higher hold a significantly higher electronic conductivity ( $\sim \times 10$ ).

For the determination of intrinsic properties of the NMC532 materials (equilibrium potential,  $D_s$ ,  $k_0$ ), a combined experimental/modeling approach using lab-made low loading electrodes is used, and it demonstrates that electrodes have minor porous electrode effects, if any, while the particle radius is determined with the material powder.

From the PITT measurement, the diffusion coefficient exhibits a strong dependency on the lithium concentration of the material, while the reaction rate constant remains constant over a large range

of the stoichiometry before declining as the full lithiation state is achieved. Different results of diffusion coefficient for similar NMC materials from literature are compared with the values in this work and show a similar tendency over the same range of stoichiometry. Therefore, to derive reliable results of the internal battery parameters, the concentration dependency of the diffusion coefficient and reaction rate constant should be considered.

Although the Newman P2D model fits well most of the current responses from the PITT measurement, the diffusion coefficient obtained from the fitting process does not allow for validating the discharge rate capability of the thin electrodes using the Newman P2D model. A diffusion coefficient from the literature is then used and adjusted for validating the discharge rate capability of the thin electrode. When the polynomial approximation assumption is adopted, i.e., Newman-pa model, it also requires an additional adjustment for the diffusion coefficient.

The validation on the discharge rate capability of a thin electrode provides a trustworthy set of parameters for the micro-scale of the Newman P2D model. Therefore, the possible discrepancy between the simulated results and the experimental data is expected to occur at the macro-scale of the model, which will be addressed in the second part of this series of papers using industry-grade electrodes.

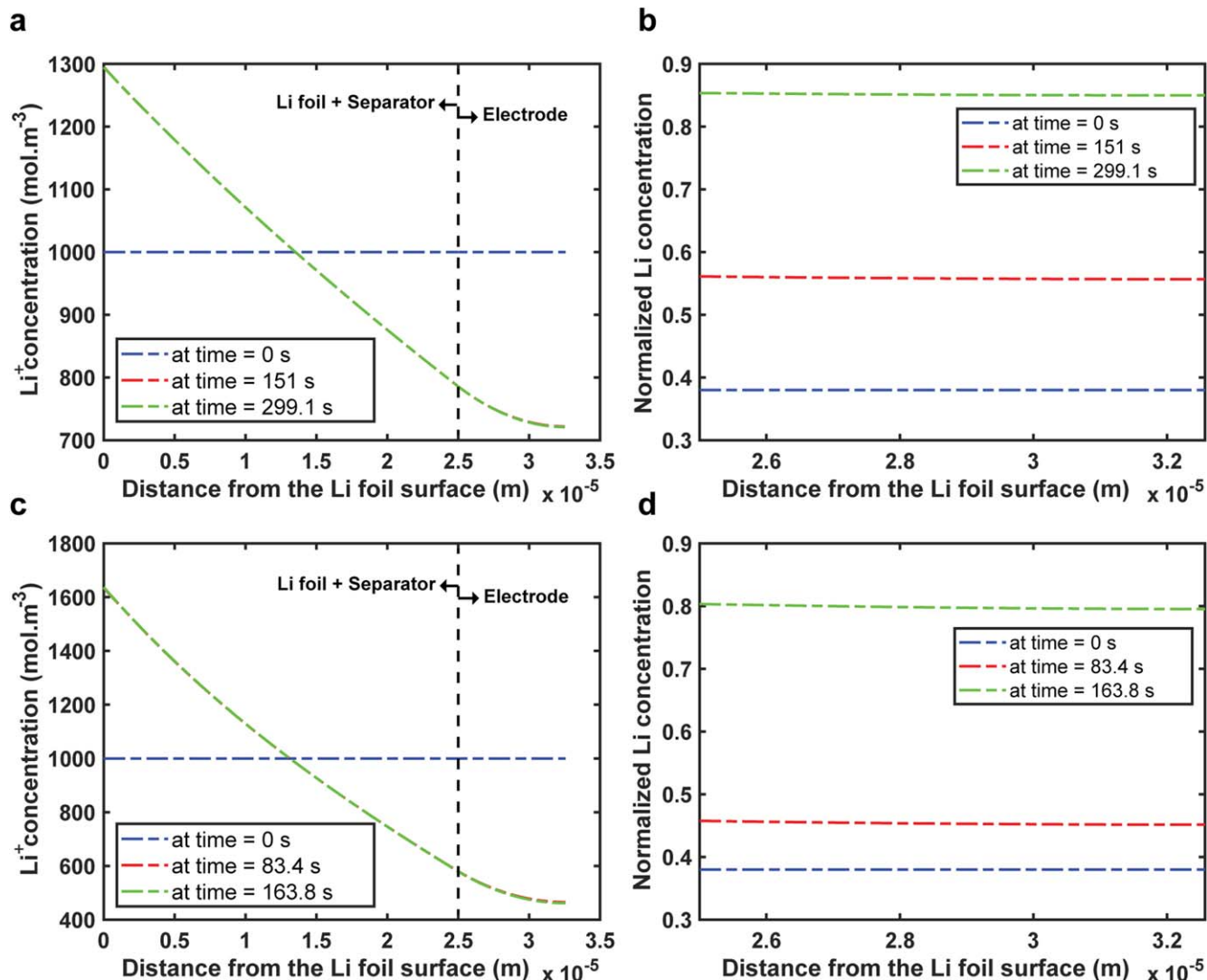


**Figure 11.** Simulated concentration profile across the low loading electrode (“model” thin electrode). (a), (c). Concentration profile at different times across the separator + PE thickness at 10 C and 20 C, respectively. (b), (d). AM utilization profile at different times across the separator + PE thickness at 10 C and 20 C, respectively.

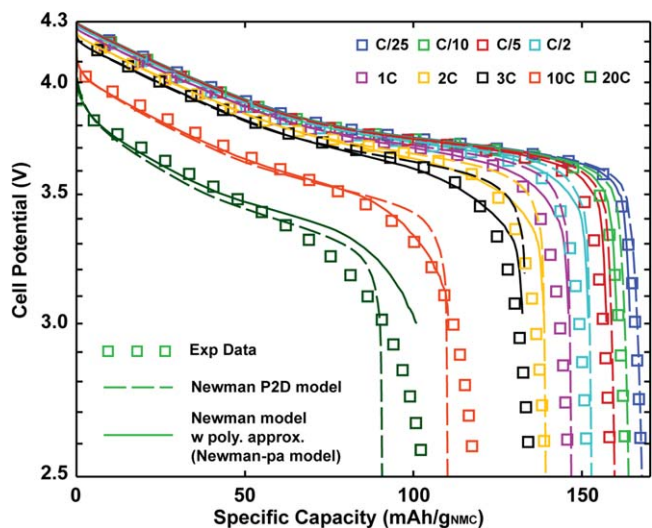


**Figure 12.** Validation on the thin electrode for polynomial approximation. The parameters for intrinsic properties of AM are validated again using the Newman model with polynomial approximation upon the rate capability of the thin electrode.

Altogether this work proposes a parameterization procedure that can be applied by model developers, to adopt their model to new materials.

### Acknowledgments

The authors would like to acknowledge French National Association for Research and Technology (ANRT) for partially supporting the funding of this research work. T.-T. Nguyen was supported by Renault Group for his PhD Project. The micro 4-line conductivity measurements was supported by the IEMN-PCMP-PCP platform and the RENATECH network.

### ORCID

Charles Delacourt <https://orcid.org/0000-0001-5241-5441>

### References

1. J. Kim, H. Lee, H. Cha, M. Yoon, M. Park, and J. Cho, *Adv. Energy Mater.*, **8**, 1702028 (2018).
2. S. T. Myung, F. Maglia, K. J. Park, C. S. Yoon, P. Lamp, S. J. Kim, and Y. K. Sun, *ACS Energy Lett.*, **2**, 196 (2017).
3. A. Manthiram, B. Song, and W. Li, *Energy Storage Mater.*, **6**, 125 (2017).
4. W. Li, E. M. Erickson, and A. Manthiram, *Nat. Energy*, **5**, 26 (2020).
5. J. Li, A. R. Cameron, H. Li, S. Glazier, D. Xiong, M. Chatzidakis, J. Allen, G. A. Botton, and J. R. Dahn, *J. Electrochem. Soc.*, **164**, A1534 (2017).

6. M. M. Forouzan, B. A. Mazzeo, and D. R. Wheeler, *J. Electrochem. Soc.*, **165**, 10 (2018).
7. S. L. Morelly, N. J. Alvarez, and M. H. Tang, *J. Power Sources*, **387**, 49 (2018).
8. H. Zheng, L. Tan, G. Liu, X. Song, and V. S. Battaglia, *J. Power Sources*, **208**, 52 (2012).
9. S. Malifarge, B. Delobel, and C. Delacourt, *J. Electrochem. Soc.*, **165**, A1275 (2018).
10. X. Lu et al., *Nat. Commun.*, **11**, 1 (2020).
11. T.-T. Nguyen, J. Villanova, Z. Su, R. Tucoulou, B. Fleutot, B. Delobel, C. Delacourt, and A. Demortière, *Adv. Energy Mater.*, **11**, 2003529 (2021).
12. R. Xu, Y. Yang, F. Yin, P. Liu, P. Cloetens, Y. Liu, F. Lin, and K. Zhao, *J. Mech. Phys. Solids*, **129**, 160 (2019).
13. L. Almar, J. Joos, A. Weber, and E. Ivers-Tiffée, *J. Power Sources*, **427**, 1 (2019).
14. D. E. Stephenson, B. C. Walker, C. B. Skelton, E. P. Gorzkowski, D. J. Rowenhorst, and D. R. Wheeler, *J. Electrochem. Soc.*, **158**, A781 (2011).
15. V. Wood, *Nat. Rev. Mater.*, **3**, 293 (2018).
16. J. Eller, M. Ebner, C. Burns, J. Dahn, and V. Wood, *J. Electrochem. Soc.*, **165**, 339 (2018).
17. M. Ebner, F. Geldmacher, F. Marone, M. Stampanoni, and V. Wood, *Adv. Energy Mater.*, **3**, 845 (2013).
18. J. Newman and W. Tiedemann, *AICHE J.*, **21**, 25 (1975).
19. T. F. Fuller, M. Doyle, and J. Newman, *J. Electrochem. Soc.*, **141**, 982 (1994).
20. K. E. Thomas, J. Newman, and R. M. Darling, "Mathematical Modeling of Lithium Batteries." *Advances in Lithium-ion Batteries* (KluwerAcademic, New York, NY) 12 (2002).
21. J. Newman and K. E. Thomas-Alyea, *Electrochemical Systems* (Wiley, New York, NY) (2012).
22. S. Malifarge, B. Delobel, and C. Delacourt, *J. Electrochem. Soc.*, **164**, A3925 (2017).
23. A. Verma, K. Smith, S. Santhanagopalan, D. Abraham, K. P. Yao, and P. P. Mukherjee, *J. Electrochem. Soc.*, **164**, A3380 (2017).
24. J. Schmalstieg, C. Rahe, M. Ecker, and D. U. Sauer, *J. Electrochem. Soc.*, **165**, A3799 (2018).
25. M. Ecker, T. K. D. Tran, P. Dechent, S. Käbitz, A. Warnecke, and D. U. Sauer, *J. of The Electrochem. Soc.*, **162**, 1836 (2015).
26. S.-L. Wu, W. Zhang, X. Song, A. K. Shukla, G. Liu, V. Battaglia, and V. Srinivasan, *J. Electrochem. Soc.*, **159**, 438 (2012).
27. C.-H. Chen, F. B. Planella, K. O'Regan, D. Gastol, W. Dhammika Widanage, and E. Kendrick, *J. Electrochem. Soc.*, **167**, 8 (2020).
28. A. M. Colclasure, A. R. Dunlop, S. E. Trask, B. J. Polzin, A. N. Jansen, and K. Smith, *J. Electrochem. Soc.*, **166**, A1412 (2019).
29. M. Doyle, J. Newman, A. S. Gozdz, C. N. Schmutz, and J. Tarascon, *J. Electrochem. Soc.*, **143**, 1890 (1996).
30. P. Albertus, J. Christensen, and J. Newman, *J. Electrochem. Soc.*, **156**, A606 (2009).
31. S.-L. Wu, D. Y. Parkinson, Y. Fu, S. Ferreira, V. Battaglia, and V. Srinivasan, *J. Electrochem. Soc.*, **164**, 3473 (2017).
32. M. Ecker, S. Käbitz, I. Laresgoiti, and D. U. Sauer, *J. of The Electrochem. Soc.*, **162**, 1849 (2015).
33. F. L. E. Usseglio-Viretta et al., *J. Electrochem. Soc.*, **165**, A3403 (2018).
34. C. Delacourt, DUMBAT,' can be found under (<http://charles.delacourt.free.fr/dumbat>, n.d).
35. V. R. Subramanian, V. D. Diwakar, and D. Tapriyal, *J. Electrochem. Soc.*, **152**, A2002 (2005).
36. J. Landesfeind, J. Hattendorff, A. Ehrl, W. A. Wall, and H. A. Gasteiger, *J. Electrochem. Soc.*, **163**, A1373 (2016).
37. S. Malifarge, B. Delobel, and C. Delacourt, *J. Electrochem. Soc.*, **164**, E3329 (2017).
38. I. Shiraki, F. Tanabe, R. Hobara, T. Nagao, and S. Hasegawa, *Surf. Sci.*, **493**, 633 (2001).
39. I. Miccoli, F. Edler, H. Pfnür, and C. Tegenkamp, *J. Phys. Condens. Matter*, **27**, 223201 (2015).
40. B. Voigtländer, V. Cherepanov, S. Korte, A. Leis, D. Cuma, S. Just, F. Lüpke, B. Voigt, and F. L. Upke, *Rev. Sci. Instrum.*, **89**, 101101 (2018).
41. H. Lundgren, M. Behm, and G. Lindbergh, *J. Electrochem. Soc.*, **162**, A413 (2015).
42. J. Landesfeind and H. A. Gasteiger, *J. Electrochem. Soc.*, **166**, A3079 (2019).
43. M. Mastali, M. Farkhondeh, S. Farhad, R. A. Fraser, and M. Fowler, *J. Electrochem. Soc.*, **163**, A2803 (2016).
44. J. Park et al., *Nat. Mater.*, **20**, 991 (2021), 2021 20721 20720.
45. 'Celgard,' can be found under (<https://celgard.com/>).
46. C. Delacourt, M. Ati, and J. M. Tarascon, *J. Electrochem. Soc.*, **158**, A741 (2011).
47. J. Li, F. Yang, X. Xiao, M. W. Verbrugge, and Y. T. Cheng, *Electrochim. Acta*, **75**, 56 (2012).
48. J. Li, X. Xiao, F. Yang, M. W. Verbrugge, and Y. T. Cheng, *J. Phys. Chem. C*, **116**, 1472 (2012).
49. M. D. Levi and D. Aurbach, *J. Phys. Chem. B*, **101**, 23 (1997).
50. C. Montella, *Electrochim. Acta*, **51**, 3102 (2006).
51. E. Markevich, M. D. Levi, and D. Aurbach, *J. Electroanal. Chem.*, **580**, 231 (2005).
52. D. R. Baker and M. W. Verbrugge, *J. Electrochem. Soc.*, **160**, A1319 (2013).
53. R. S. Nicholson and I. Shain, *Anal. Chem.*, **36**, 706 (1964).
54. Q. Guo, V. R. Subramanian, J. W. Weidner, and R. E. White, *J. Electrochem. Soc.*, **149**, A307 (2002).
55. G. Sikha and R. E. White, *J. Electrochem. Soc.*, **154**, A43 (2007).
56. I. V. Thorat, D. E. Stephenson, N. A. Zacharias, K. Zaghbi, J. N. Harb, and D. R. Wheeler, *J. Power Sources*, **188**, 592 (2009).
57. F. Pouraghajan, H. Knight, M. Wray, B. Mazzeo, R. Subbaraman, J. Christensen, and D. Wheeler, *J. Electrochem. Soc.*, **165**, 2644 (2018).
58. T.-T. Nguyen, A. Demortière, B. Fleutot, B. Delobel, C. Delacourt, and S. J. Cooper, *NPJ Comput. Mater.*, **6**, 1 (2020).
59. S. J. Cooper, A. Bertei, P. R. Shearing, J. A. Kilner, and N. P. Brandon, *SoftwareX*, **5**, 203 (2016).
60. S. W. Peterson and D. R. Wheeler, *J. Electrochem. Soc.*, **161**, A2175 (2014).
61. H. Zheng, R. Yang, G. Liu, X. Song, and V. S. Battaglia, *J. Phys. Chem. C*, **116**, 4875 (2012).
62. S. J. Tambio, F. Cadiou, E. Maire, N. Besnard, M. Deschamps, and B. Lestriez, *J. Electrochem. Soc.*, **167**, 160509 (2020).
63. F. Cadiou, T. Douillard, N. Besnard, B. Lestriez, and E. Maire, *J. Electrochem. Soc.*, **167**, 10 (2020).
64. R. Amin and Y.-M. Chiang, *J. Electrochem. Soc.*, **163**, A1512 (2016).